Journal of Materials Chemistry A

Accepted Manuscript

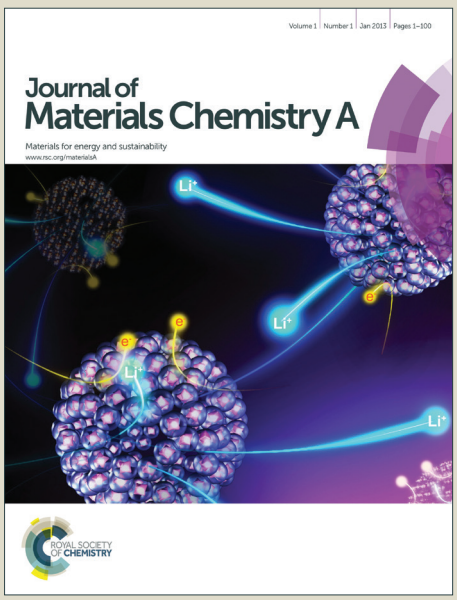

ROYAL SOCIETY OF CHEMISTRY

www.rsc.org/materialsA

Graphical Abstract

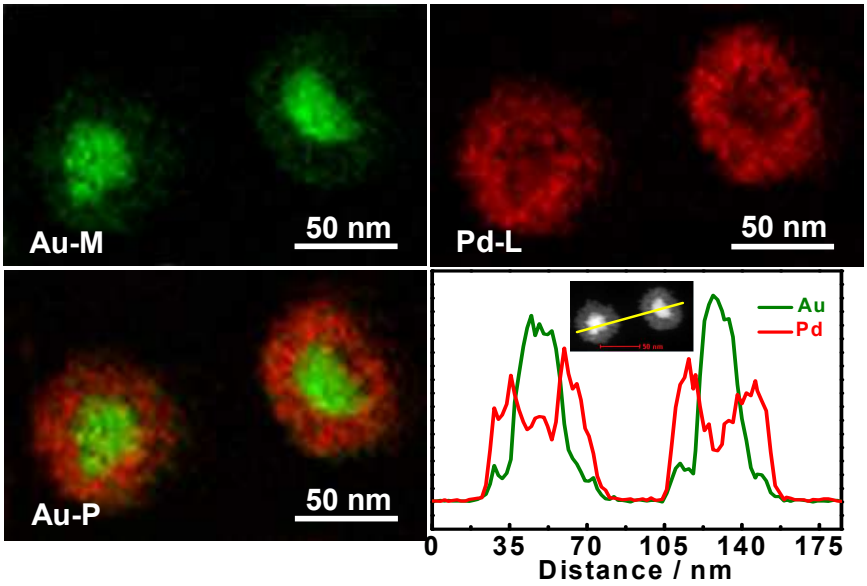

A simple, seed-less, and one-pot wet-chemical route was designed for synthesis of well-dispersed gold@palladium core-shell nanoflowers supported on reduced graphene oxide. The as-prepared Au@Pd/rGO exhibited the enhanced electrocatalytic activity and better stability for ORR and ethylene glycol oxidation in alkaline media.

One-step seed-less wet-chemical synthesis of gold@palladium nanoflowers supported on reduced graphene oxide with enhanced electrocatalytic properties

Shan-Shan Li, Ai-Jun Wang, Yuan-Yuan Hu, Ke-Ming Fang, Jian-Rong Chen, Jiu-Ju Feng*

College of Chemistry and Life Science, College of Geography and Environmental Science, Zhejiang Normal University, Jinhua, 321004, China

**Corresponding author: jjfeng@zjnu.cn (JJF).*

Abstract

Herein, a simple one-step seed-less wet-chemical method was developed for synthesis of well-dispersed gold@palladium core-shell nanoflowers supported on reduced graphene oxide (Au@Pd/rGO), with the assistance of melamine as a linker agent, using poly(vinylpyrrolidone) as a structure-directing agent. The as-prepared Au@Pd/rGO exhibited enhanced electrocatalytic activity and better stability for oxygen reduction reaction (ORR) and ethylene glycol (EG) oxidation in alkaline media, compared with Pd/rGO, Au/rGO, and Pd black. This method can be extended to facilely prepare core-shell nanostructures with designed compositions and desired catalytic properties.

Keywords: Reduced graphene oxide; Core-shell nanoflowers; Melamine; Oxygen reduction reaction; Ethylene glycol oxidation

1 Introduction

Recently, ethylene glycol (EG) has attracted increasing attention in fuel cells because of its low toxicity, high boiling point, high energy density, and relatively high reactivity.[1-3] Oxygen reduction reaction (ORR) are recognized as the kinetically limiting step in fuel cells, owing to its sluggish reaction kinetics.[4, 5] And a high ORR overpotential is the main obstacle to limit the potential commercialization. Therefore, many efforts have been devoted to search cost-effective and efficient catalysts.[6-8] Particularly, platinum (Pt), as the most efficient electrocatalyst, is severely inhibited from potential commercialization for its high cost, poor stability, and weak poison resistance.[8-10] It is well documented that the overpotential for ORR would be significantly reduced in alkaline media, thus offering the possibilities for low usage and broad selection of electrocatalysts instead of Pt for catalytic reactions.[11, 12] It facilitates the development of non-Pt-based electrocatalysts for fuel cells in alkaline media.

Recently, palladium (Pd) catalysts, as a substitute for Pt catalysts, were found to have competitive intrinsic electrocatalytic performances in fuel cells, compared with Pt-based catalysts.[13, 14] Furthermore, incorporating other transition metals with Pd demonstrates the great improvement of catalytic performances and the reduction of Pd loading, owing to their remarkable synergistic catalytic effects.[15, 16] Tan et al. prepared many CuPd nanostructures by simultaneously reducing copper(II) acetylacetonate ($Cu(acac)_2$) and palladium(II) acetylacetonate ($Pd(acac)_2$), which exhibited the enhanced electrocatalytic activities, as compared to Pt/C.[17] Yin and coworkers

fabricated Pd-Fe alloyed nanoparticles supported on tungsten carbide, which displayed a comparable ORR activity to Pt/C.[18] Xu' group synthesized nanoporous PdNi alloys, which showed higher electrocatalytic activity toward ORR than those of Pt/C and Pd nanoparticles.[19] Nevertheless, the above methods usually suffer from relatively high cost, rigorous reaction conditions and operation skills, and poor reproducibility. Thus, it is essential to develop a facile strategy to search highly active Pd-based nanocatalysts with high catalytic activity and structure durability.

It is known that the electrocatalytic performance strongly depends on the compositions and/or structural features of a catalyst from practical catalysis viewpoint.[20-22] Core-shell nanostructures with designed compositions represent a highly interesting class of catalysts,[23, 24] especially for Pd-based core-shell nanostructures because of their significantly enhanced catalytic activities. For example, Shao and co-workers prepared a core-shell catalyst consisting of a nanoporous PdNi core with enhanced catalytic activity for ORR.[25] In another example, Zhang and co-workers synthesized hexagonal shield-shaped Au@Pd core-shell nanocrystals using Au triangular plates as the structure-directing cores, which exhibited the improved electrocatalytic activity for ethanol oxidation.[26] Despite the impressive advances in the design of multi-composition core-shell nanostructures, core-shell-structured catalysts are usually prepared by a multistep seed-mediated growth method, in which the particle size and shape are uncontrollable in the absence of pre-formed uniform seeds.[21, 27, 28] As a result, their large-scaled synthesis is severely limited.

Bimetallic nanostructures usually suffer from heavy aggregation during the synthetic process and their repeated use in catalysis reactions.[2, 29] These issues can be efficiently overcome by introducing graphene as supporting material, because graphene has two-dimensional nanostructures, large specific surface area, good electrical conductivity, and unique chemical property.[30, 31]

In this report, we demonstrated a one-step effective route for synthesis of Au@Pd core-shell nanoflowers supported on reduced graphene oxide (rGO, Au@Pd/rGO) in aqueous media. The electrocatalytic properties of Au@Pd/rGO were investigated in some detail, using ORR and EG oxidation as bench-model systems.

2 Results and discussion

2.1 Characterization

Morphology of the typical product was characterized by transmission electron microscopy (TEM). Fig. 1 shows that the product contains a lot of well-dispersed nanoflowers deposited on rGO with high density and narrow size distribution (inset in Fig. 1B) from 40 to 48 nm (average size of 44 nm), which are quite different from Au/rGO and Pd/rGO (Fig. S1A and B, Supporting Information, SI).

The crystalline nature of the sample was demonstrated by selective area electron diffraction (SAED) and high-resolution TEM (HR-TEM) measurements (inset in Fig. 1B and Fig. 2). The SAED pattern shows bright discrete diffraction spots recorded from a single nanoflower, which are indexed to the crystal planes of the face-centered cubic (fcc) Au and Pd,[32, 33] indicating high crystallinity of the product. HR-TEM

images further confirm its good crystallization. HR-TEM image exhibits clear lattice fringes of the marked regions with the interplanar spacings of 0.230 nm and 0.200 nm corresponding to the (111) and (200) planes of the fcc Au and Pd, respectively.[32, 33]

Fig. 3 shows the elemental mapping images of the as-prepared nanoflowers recorded by high-angle annular dark-field scanning transmission electron microscopy energy dispersive X-ray spectroscopy (HAADF-STEM-EDS). It clearly reveals that Au is concentrated in the core, while Pd is externally distributed throughout the entire nanoflowers. This observation is strongly manifested by cross-sectional compositional line profiles with Au and Pd elements (Fig. 3D), showing the formation of Au@Pd nanoflowers. Additionally, the metal loading of Au@Pd nanoflowers on rGO is measured to be 31 wt % by thermogravimetric analysis (TGA, Fig. S2, SI).

The crystalline structure of Au@Pd/rGO was examined by X-ray diffraction (XRD) pattern (Fig. 4, curve a). There are four typical diffraction peaks located at 38.45°, 44.82°, 65.24°, and 79.84°, which are indexed to the reflections of the fcc structure of metal. Notably, each diffraction peak has an asymmetric line shape inclined toward higher-angle direction, compared with that of Au/rGO (curve b). This is attributed to synergistic effects of Au and Pd, in good accordance with previous observations in the literature.[34, 35] Furthermore, a broad diffraction peak at 22.85° is observed for Au@Pd/rGO (curve a), Au/rGO (curve b), and Pd/rGO (curve c), which is quite different from that of GO (curve d) only with a strong peak emerged at 10.84°. These phenomena indicate the efficient reduction of GO to rGO in the present system.

X-ray photoelectron spectroscopy (XPS) was employed to examine the

compositions and surface oxidation states of Au@Pd/rGO. As illustrated in Fig. 5A, the dominant XPS peaks at 85.58, 284.33, 337.65, 398.97, and 531.55 eV come from Au 4f, C 1s, Pd 3d, N 1s, and O 1s in the survey spectrum, respectively. Fig. 5B shows the peak fitting of high-resolution C 1s region. There are two peaks at 283.91 and 286.45 eV corresponding to the sp^2-hybridized graphene C–C and C–O groups, respectively.[36, 37] The sp^2-hygridized graphene C–C peaks are assigned to graphitic structure.[38] The peaks of oxygen containing functional groups become lower while the intensity of C–C peaks is stronger for Au@Pd/rGO, different from that of GO under the similar conditions (Fig. S3A, SI). These observations evidence the efficient reduction of GO to rGO. In addition, the C–N peaks at 285.03 eV are attributed to the amino functional nitrogenous heterocycle, showing the critical role of melamine as a linker agent.[36]

Fig. 5C shows Au $4f_{7/2}$ and Au $4f_{5/2}$ doublet with the binding energies of 83.16 and 86.83 eV, respectively, corresponding to metallic Au.[33, 39] The Pd $3d_{5/2}$ and Pd $3d_{3/2}$ peaks emerged at 334.70 and 340.03 eV are originated from metallic Pd (Fig. 5D).[39, 40] The binding energies of Au 4f and Pd 3d both show slight negative shift, compared to Au 4f of Au/rGO and Pd 3d of Pd/rGO (Fig. S3B and C, SI). It means a slight change occurred in the electronic properties of Au and Pd.[33] Additionally, estimating from the relative peak intensity, the atomic ratio of Au to Pd is about 1:1, which is well consistent with the molar ratio of the precursors.

Fourier transform infrared (FT-IR) spectroscopy was employed to further investigate the functional groups in Au@Pd/rGO. As shown in Fig. S4 (SI), there are

two dominant peaks at 1626 and 3432 cm^{-1} in each sample, which are come from the C=C skeletal vibration of the sp^2-hybridized carbon atoms,[41] and O–H stretching vibration of the C–OH groups and water[42], respectively. The oxygen containing functional groups in Au@Pd/rGO (curve a), Pd/rGO (curve b), and Au/rGO (curve c) are weaker in contrast to that of GO (curve d), demonstrating the effective reduction of GO. In the FT-IR spectra of Au@Pd/rGO (curve a), Pd/rGO (curve b), and Au/rGO (curve c), there is one additional absorption peak observed at 1273 cm^{-1} corresponding to the stretching vibration of C–N groups, further confirming the linker role of melamine.[36] These results agree well with the XPS data.

In the present synthesis, the use of melamine, PVP, and GO were critical for the formation of well-dispersed Au@Pd nanoflowers with high quality. Specifically, the absence of melamine fails to yield Au@Pd nanoflowers, although other conditions are kept constant (Fig. S5A, SI). Moreover, the absence of PVP induces the formation of flower-like nanostructures with decreased quality and density (Fig. S5B, SI). Additionally, the nanoflowers are severely aggregated together without GO (Fig. S5C, SI).

Furthermore, we found that the reaction temperature is also important to synthesize Au@Pd nanoflowers with good dispersity and high quality. Decreasing the temperature from 60 ºC to 40 ºC (Fig. S6B, SI) and even 25 ºC (Fig. S6A, SI), by increasing the reaction time to several hours and even one day, produces nanoflowers and irregular solid nanoparticles with poor quality, respectively. Alternatively, as the temperature increased to 80 ºC, a lot of nanodendrites are emerged, rather than

nanoflowers (Fig. S6C, SI).

The formation mechanism of Au@Pd/rGO can be explained by a three-staged growth model: N-doped rGO, nucleation, and anisotropic growth. Melamine, as a nitrogenous heterocyclic compound with amino functional groups, can adsorb onto the inherently hydrophobic surfaces of rGO via π-π stacking.[43, 44] Thus, $AuCl_4^-$ and $PdCl_4^{2-}$ would attract the sterically accessible nitrogen atoms by electrostatic self-assembly, leading to the uniform distribution of $AuCl_4^-$ and $PdCl_4^{2-}$ on the surface of rGO, as strongly supported by the previous work.[44-46]

After the addition of formic acid, the adsorbed $AuCl_4^-$ and $PdCl_4^{2-}$ would be in-situ reduced accordingly. The reduction of $AuCl_4^-$ preferentially occurs at the very early stage, because the standard reduction potential of $AuCl_4^-$/Au (0.930 V *vs*. SHE) is slightly higher than that of $PdCl_4^{2-}$/Pd (0.915 V *vs*. SHE). The newly generated Au atoms serve as seeds for subsequent deposition of Pd atoms. Meanwhile, Pd atoms are inclined to occupy the surface of metallic nanocrystal.[33] As a result, spontaneous separation occurs between interior Au and exterior Pd in the present system.

During the later anisotropic growth of Pd, PVP acts as a structure-directing agent,[40, 47, 48] inducing the formation of AuPd nanoflowers. After the careful removal of PVP with water and ethanol, Au@Pd/rGO nanocomposites were obtained finally, as described in Fig. 6.

2.2 Electrocatalytic reduction of oxygen

Cyclic voltammetry (CV) curves were used for preliminary study of the

electrochemical properties of Au@Pd/rGO (curve a) modified electrode, using Pd/rGO (curve b), Pd black (curve c), and Au/rGO (curve d) as references (Fig. 7A). The CV curves are consistent with the typical characterized CV regions of Pd/Au: typical hydrogen adsorption/desorption peaks in the potential range of –0.9 ~ –0.6 V, double-layer capacitance region from –0.6 to –0.4 V, and metal oxidation/reduction peaks from –0.4 to 0.1 V.[36, 49, 50] Because hydrogen can penetrate into the Pd lattices, the electrochemically active surface area (ECSA) of Pd-based catalysts were calculated based on the charges of the reduction region of PdO/Pd at around –0.25 V, subtracting the double-layer correction and assuming 0.405 mC cm^{-2} for the reduction of a monolayer of PdO on the catalyst surface.[12, 51] The ECSA of Au@Pd/rGO is 67.6 m^2 g^{-1}, which is much larger than that of Pd/rGO (61.6 m^2 g^{-1}) and Pd black (24.2 m^2 g^{-1}), owing to serious agglomeration of Pd black (Fig. S7, SI). The unique porous structures of Au@Pd/rGO provide reasonably enlarged surface areas.

Fig. 7B shows the ORR polarization curves of Au@Pd/rGO (curve a), Pd/rGO (curve b), Pd black (curve c), and Au/rGO (curve d) modified electrodes. All the polarization curves display a diffusion-limited current region from –0.80 to –0.40 V and a mixed kinetics-diffusion control region from –0.40 to –0.05 V. The onset potential (–0.05 V) and half-wave potential (–0.25 V) for Au@Pd/rGO are much more positive than those of the other catalysts. Meanwhile, the mass activities of the four catalysts at –0.70 V are provided for comparison (Fig. 7C). Notably, the mass activity is 85 mA mg^{-1} for Au@Pd/rGO, which is much higher than those of Pd/rGO (80 mA mg^{-1}), Pd black (48 mA mg^{-1}), and Au/rGO (17 mA mg^{-1}). All these results

indicate the enhanced ORR activity of Au@Pd/rGO in alkaline media.

Chronoamperometric tests were conducted to determine the durability of the catalysts for ORR. As shown in Fig. 7D, Au@Pd/rGO modified electrodes have the higher initial current, much lower deterioration rate, and higher reduction current than those of the other catalysts under the same conditions, confirming the better stability of Au@Pd/rGO.

To obtain the kinetics of ORR, the polarization curves were recorded at various rotation rates (Fig. 8A). Based on the polarization curves at different potentials, we drafted the corresponding Koutecky-Levich plots (Fig. 8B). The electron transfer number involved per O_2 molecule reduction can be determined from the Koutecky-Levich equation. The electron transfer number is around 4.0 ~ 4.4, revealing that ORR is mainly dominated by a four-electron pathway for Au@Pd/rGO, and O_2 is directly reduced to H_2O.

To further examine the stability of Au@Pd/rGO, the repeated ORR polarization curves performed 1000 times in O_2 saturated 0.1 M KOH at a scan rate of 10 mV s^{-1}, using a rotation rate of 1600 rpm (Fig. 8C). After the durability test, nearly identical polarization curve was observed in terms of the onset potential, half-wave potential, and limiting current, evidencing the improved stability of Au@Pd/rGO, as demonstrated by the chronoamperometric measurements.

In direct methanol fuel cells (DMFCs), methanol tolerance for ORR is a great challenge because methanol permeation to the cathode will dramatically degrade the power density of fuel cells.[52] As a result, it is of practical significance for the cathode

catalysts to possess methanol tolerance. The ORR activity of Au@Pd/rGO was also examined in the presence of methanol. As shown in Fig. 8D, the half-wave potential has little degradation in the presence of methanol, as well as almost constant current density, compared to that without methanol, indicating the improved ORR activity for Au@Pd/rGO in the presence of methanol. The superior methanol tolerance makes Au@Pd/rGO a preferable ORR catalyst in DMFCs.

2.3 Electrocatalytic activity for EG oxidation

To further evaluate the catalytic performance of the as-prepared Au@Pd/rGO, the electrooxidation of EG was performed. Fig. 9A shows the CV curves of Au@Pd/rGO (curve a), Pd/rGO (curve b), Pd black (curve c), and Au/rGO (curve d) modified electrodes. Clearly, the four catalysts display the similar feature. Specifically, there are one typical EG oxidation peak in the forward scan and another oxidation peak in the reverse scan corresponding to the removal of the residual carbonaceous species formed in the forward scan.[8, 37] The current density of Au@Pd/rGO is about 77.5 mA cm^{-2}, which is 2.4, 1.5, and 37 times of those of Pd/rGO (32.6 mA cm^{-2}), Pd black (53.0 mA cm^{-2}), and Au/rGO (2.1 mA cm^{-2}). And the onset potential (–0.55 V) and peak potential (–0.094 V) of Au@Pd/rGO are more negative than the references.

More importantly, the ratio of the forward peak current density (j_F) to the reverse one (j_R), denoted as j_F/j_R, can be used to describe the catalyst tolerance to the ccumulated carbonaceous species.[53] A low j_F/j_R value means poor oxidation of EG to CO during the forward scan and excessive accumulation of residual carbonaceous

species on the catalyst surface, revealing a greater extent of CO poisoning.[53] The ratio of j_F/j_R is 2.85 for Au@Pd/rGO, which is larger than Pd/rGO (1.89), Pd black (2.18), and Au/rGO (1.6), respectively, evidencing the best CO resistance of Au@Pd/rGO among the four catalysts.

The durability of Au@Pd/rGO modified electrode for EG oxidation was firstly evaluated through the chronoamperometric measurements at the applied potential of –0.1 V (Fig. 9B), using Pd/rGO (curve b), Pd black (curve c), and Au/rGO (curve d) modified electrodes as standards. Evidently, Au@Pd/rGO modified electrode shows much higher catalytic current density and slower degradation under the identical conditions, demonstrating higher catalytic activity and better stability than those of the other catalysts. Additionally, the initial currents drop quickly for the four catalysts, owing to the formation of the intermediate carbonaceous species during EG oxidation.[53]

The stability of Au@Pd/rGO was further investigated in 0.1 M KOH containing 0.5 M EG. It can be observed that the current densities decrease gradually with successive scans (Fig. 9C). Using j_F of the 5th cycle as a reference, the j_F at Au@Pd/rGO modified electrode remains about 75% after 100 cycles (inset in Fig. 9C). Besides, the peak potential are located in the range of –0.094 ~ –0.092 V for EG oxidation. Furthermore, the j_F/j_R ratios are enlarged with the value above 2.65 for EG oxidation on Au@Pd/rGO modified electrode during the accelerated durability test (Fig. 9D). These results further demonstrate the enhanced stability and strong CO tolerance of Au@Pd/rGO.

In control experiments, the electrocatalytic activity of N-doped rGO modified by malemine was provided for comparison, using pure rGO as a standard. As exhibited in Fig. S8 (SI), N-doped rGO modified electrode shows better catalytic activity in comparison with rGO, indicating that the existence of melamine is benefit to the superior activity of Au@Pd/rGO due to the higher activity of N-doped carbons.

3. Conclusions

In summary, a simple, seed-less, and one-step wet-chemical route was developed for synthesis of Au@Pd/rGO, with the assistance of melamine as a cross-linker agent and PVP as a structure-directing agent. The as-prepared product showed the enhanced electrocatalytic activity and better stability for ORR and EG oxidation in alkaline media, compared to Pd black, Pd/rGO, and Au/rGO. The improved performance is attributed to the unique porous structures, N-doped rGO support, and the changes in the electronic structures as Au is doped by Pd. This method would be used to synthesize other Pd-based electrocatalysts with low cost and high catalytic performance for fuel cells.

Acknowledgements

This work was financially supported by National Natural Science Foundation of China (No. 21475118, 21175118, 21275130, and 21275131), and Zhejiang province university young academic leaders of academic climbing project (No. pd2013055).

References

1 H. Wang, Z. Jusys and R. J. Behm, *Electrochim. Acta*, 2009, **54**, 6484-6498.

2 S.-S. Li, Y.-Y. Hu, J.-J. Feng, Z.-Y. Lv, J.-R. Chen and A.-J. Wang, *Int. J. Hydrogen Energy*, 2014, **39**, 3730-3738.

3 V. Livshits and E. Peled, *J. Power Sources*, 2006, **161**, 1187-1191.

4 G. Wu, N. H. Mack, W. Gao, S. Ma, R. Zhong, J. Han, J. K. Baldwin and P. Zelenay, *ACS nano*, 2012, **6**, 9764-9776.

5 M. K. Debe, *Nature*, 2012, **486**, 43-51.

6 G. Wu, K. L. More, C. M. Johnston and P. Zelenay, *Science*, 2011, **332**, 443-447.

7 J. Suntivich, H. A. Gasteiger, N. Yabuuchi, H. Nakanishi, J. B. Goodenough and Y. Shao-Horn, *Nat. Chem.*, 2011, **3**, 546-550.

8 J.-N. Zheng, S.-S. Li, X. Ma, F.-Y. Chen, A.-J. Wang, J.-R. Chen and J.-J. Feng, *J. Power Sources*, 2014, **262**, 270-278.

9 S. Wang, E. Iyyamperumal, A. Roy, Y. Xue, D. Yu and L. Dai, *Angew. Chem. Int. Ed.*, 2011, **50**, 11756-11760.

10 J.-J. Lv, S.-S. Li, J.-N. Zheng, A.-J. Wang, J.-R. Chen and J.-J. Feng, *Int. J. Hydrogen Energy*, 2014, **39**, 3211-3218.

11 R. C. Sekol, X. Li, P. Cohen, G. Doubek, M. Carmo and A. D. Taylor, *Appl. Catal., B*, 2013, **138**, 285-293.

12 Z. Zhang, K. L. More, K. Sun, Z. Wu and W. Li, *Chem. Mater.*, 2011, **23**, 1570-1577.

13 C. Zhu, S. Guo and S. Dong, *Adv. Mater.*, 2012, **24**, 2326-2331.

14 J.-N. Zheng, M. Zhang, F.-F. Li, S.-S. Li, A.-J. Wang and J.-J. Feng, *Electrochim. Acta*, 2014, **130**, 446-452.

15 Y. Liu and C. Xu, *ChemSusChem*, 2013, **6**, 78-84.

16 Y.-C. Wei, T.-Y. Chen, C.-W. Liu, T.-S. Chan, J.-F. Lee, C.-H. Lee, T.-L. Lin and K.-W. Wang, *Catal. Sci. Technol.*, 2012, **2**, 1654-1664.

17 L. Zhang, F. Hou and Y. Tan, *Chem. Commun.*, 2012, **48**, 7152-7154.

18 S. Yin, M. Cai, C. Wang and P. K. Shen, *Energy Environ. Sci.*, 2011, **4**, 558-563.

19 C. Xu, Y. Liu, Q. Hao and H. Duan, *J. Mater. Chem. A*, 2013, **1**, 13542-13548.

20 Z. Liu, G. S. Jackson and B. W. Eichhorn, *Angew. Chem. Int. Ed.*, 2010, **49**, 3173-3176.

21 C. Wang, W. Tian, Y. Ding, Y.-Q. Ma, Z. L. Wang, N. M. Markovic, V. R. Stamenkovic, H. Daimon and S. Sun, *J. Am. Chem. Soc.*, 2010, **132**, 6524-6529.

22 M. T. M. Koper, *Nanoscale*, 2011, **3**, 2054-2073.

23 J.-M. Yan, X.-B. Zhang, T. Akita, M. Haruta and Q. Xu, *J. Am. Chem. Soc.*, 2010, **132**, 5326-5327.

24 L. Wang and Y. Yamauchi, *J. Am. Chem. Soc.*, 2010, **132**, 13636-13638.

25 M. Shao, B. H. Smith, S. Guerrero, L. Protsailo, D. Su, K. Kaneko, J. H. Odell, M. P. Humbert, K. Sasaki, J. Marzullo and R. M. Darling, *Phys. Chem. Chem. Phys.*, 2013, **15**, 15078-15090.

26 L.-F. Zhang and C.-Y. Zhang, *Nanoscale*, 2013, **5**, 6074-6080.

27 V. Mazumder, M. Chi, K. L. More and S. Sun, *J. Am. Chem. Soc.*, 2010, **132**, 7848-7849.

28 V. Mazumder, M. Chi, K. L. More and S. Sun, *Angew. Chem. Int. Ed.*, 2010, **49**, 9368-9372.

29 J. Wang, G. Yin, H. Liu, R. Li, R. L. Flemming and X. Sun, *J. Power Sources*, 2009, **194**, 668-673.

30 S. Guo and S. Dong, *Chem. Soc. Rev.*, 2011, **40**, 2644-2672.

31 X. Huang, X. Qi, F. Boey and H. Zhang, *Chem. Soc. Rev.*, 2012, **41**, 666-686.

32 L.-F. Zhang, S.-L. Zhong and A.-W. Xu, *Angew. Chem. Int. Ed.*, 2013, **52**, 645-649.

33 J. Chai, F. Li, Y. Hu, Q. Zhang, D. Han and L. Niu, *J. Mater. Chem.*, 2011, **21**, 17922-17929.

34 D. Kim, Y. W. Lee, S. B. Lee and S. W. Han, *Angew. Chem. Int. Ed.*, 2012, **51**, 159-163.

35 Y. W. Lee, M. Kim, Z. H. Kim and S. W. Han, *J. Am. Chem. Soc.*, 2009, **131**, 17036-17037.

36 W. He, H. Jiang, Y. Zhou, S. Yang, X. Xue, Z. Zou, X. Zhang, D. L. Akins and H. Yang, *Carbon*, 2012, **50**, 265-274.

37 S.-S. Li, J.-N. Zheng, X. Ma, Y.-Y. Hu, A.-J. Wang, J.-R. Chen and J.-J. Feng, *Nanoscale*, 2014, **6**, 5708-5713.

38 J. Y. Park and S. Kim, *Int. J. Hydrogen Energy*, 2013, **38**, 6275-6282.

39 F. Li, Y. Guo, R. Li, F. Wu, Y. Liu, X. Sun, C. Li, W. Wang and J. Gao, *J.Mater. Chem. A*, 2013, **1**, 6579-6587.

40 J.-J. Lv, J.-N. Zheng, S.-S. Li, L.-L. Chen, A.-J. Wang and J.-J. Feng, *J. Mater.*

Chem. A, 2014, **2**, 4384-4390.

41 W. Yue, Z. Lin, S. Jiang and X. Yang, *J. Mater. Chem.*, 2012, **22**, 16318-16323.

42 S.-S. Li, J.-J. Lv, L.-N. Teng, A.-J. Wang, J.-R. Chen and J.-J. Feng, *ACS Appl. Mater. Interfaces*, 2014, **6**, 10549-10555.

43 S. Wang, X. Wang and S. P. Jiang, *Langmuir*, 2008, **24**, 10505-10512.

44 C. Hu, Y. Cao, L. Yang, Z. Bai, Y. Guo, K. Wang, P. Xu and J. Zhou, *Appl. Surf. Sci.*, 2011, **257**, 7968-7974.

45 S. Jiang, Y. Ma, G. Jian, H. Tao, X. Wang, Y. Fan, Y. Lu, Z. Hu and Y. Chen, *Adv. Mater.*, 2009, **21**, 4953-4956.

46 D. Wang, S. Lu and S. P. Jiang, *Electrochim. Acta*, 2010, **55**, 2964-2971.

47 J.-J. Lv, J.-N. Zheng, Y.-Y. Wang, A.-J. Wang, L.-L. Chen and J.-J. Feng, *J. Power Sources*, 2014, **265**, 231-238.

48 L. Wang and Y. Yamauchi, *Chem. Mater.*, 2011, **23**, 2457-2465.

49 M. Wang, W. Zhang, J. Wang, D. Wexler, S. D. Poynton, R. C. T. Slade, H. Liu, B. Winther-Jensen, R. Kerr, D. Shi and J. Chen, *ACS Appl. Mater. Interfaces*, 2013, **5**, 12708-12715.

50 Y. Lu, Y. Jiang, H. Wu and W. Chen, *J. Phys. Chem. C*, 2013, **117**, 2926-2938.

51 S. T. Nguyen, H. M. Law, H. T. Nguyen, N. Kristian, S. Wang, S. H. Chan and X. Wang, *Appl. Catal., B*, 2009, **91**, 507-515.

52 X. Zhao, M. Yin, L. Ma, L. Liang, C. Liu, J. Liao, T. Lu and W. Xing, *Energy Environ. Sci.*, 2011, **4**, 2736-2753.

53 J.-J. Feng, D.-L. Zhou, H.-X. Xi, J.-R. Chen and A.-J. Wang, *Nanoscale*, 2013, **5**,

6754-6757.

Captions

Fig. 1 (A, B) TEM images of Au@Pd/rGO. Insets show the corresponding particle size distribution and SAED pattern.

Fig. 2 HR-TEM images of Au@Pd/rGO.

Fig. 3 HAADF-STEM-EDS elemental mapping images (A-C) and cross-sectional compositional line profiles (D) taken from Au@Pd nanoflowers. Inset shows the corresponding HAADF-STEM image.

Fig. 4 XRD patterns of Au@Pd/rGO (curve a), Au/rGO (curve b), Pd/rGO (curve c), and GO (curve d).

Fig. 5 XPS survey (A), and high-resolution C 1s (B), Au 4f (C), and Pd 3d (D) XPS spectra of Au@Pd/rGO.

Fig. 6 Schematic illustration of the formation mechanism of Au@Pd/rGO.

Fig. 7 (A) CV curves of Au@Pd/rGO (curve a), Pd/rGO (curve b), Pd black (curve c), and Au/rGO (curve d) modified electrodes in 0.1 M KOH at a scan rate of 50 mV s^{-1}. ORR polarization curves (B) and chronoamperometric curves (D) of Au@Pd/rGO (curve a), Pd/rGO (curve b), Pd black (curve c), and Au/rGO (curve d) modified

electrodes in O_2 saturated 0.1 M KOH at a rotation rate of 1600 rpm. (C) The corresponding mass activities at –0.7 V.

Fig. 8 (A) ORR polarization curves of Au@Pd/rGO modified electrodes in O_2 saturated 0.1 M KOH at a scan rate of 10 mV s^{-1} and various rotation rates (curve a-e): 100, 400, 900, 1600, and 2500 rpm. (B) The corresponding Koutecky-Levich plots at different potentials. (C) The corresponding ORR polarization curves before and after the accelerated durability test. (D) ORR polarization curves of Au@Pd/rGO modified electrode in O_2 saturated 0.1 M KOH with and without 0.1 M methanol at a scan rate of 10 mV s^{-1}, using a rotation rate of 1600 rpm.

Fig. 9 (A) CV curves of Au@Pd/rGO (curve a), Pd/rGO (curve b), Pd black (curve c), and Au/rGO (curve d) modified electrodes in 0.1 M KOH + 0.5 M EG at a scan rate of 50 mV s^{-1}. (B) Chronoamperometric curves of Au@Pd/rGO (curve a), Pd/rGO (curve b), Pd black (curve c), and Au/rGO (curve d) modified electrodes in 0.1 M KOH + 0.5 M EG. (C) Forward peak current density (j_F) as a function of potential scanning cycles of Au@Pd/rGO modified electrode in 0.1 M KOH + 0.5 M EG at a scan rate of 50 mV s^{-1}. Inset shows the CV curves of the corresponding 5th and 100th cycles. (D) The corresponding changes of the ratios of the forward peak current density (j_F) to the reverse one (j_R) for the oxidation of EG.

Figures

Fig. 1

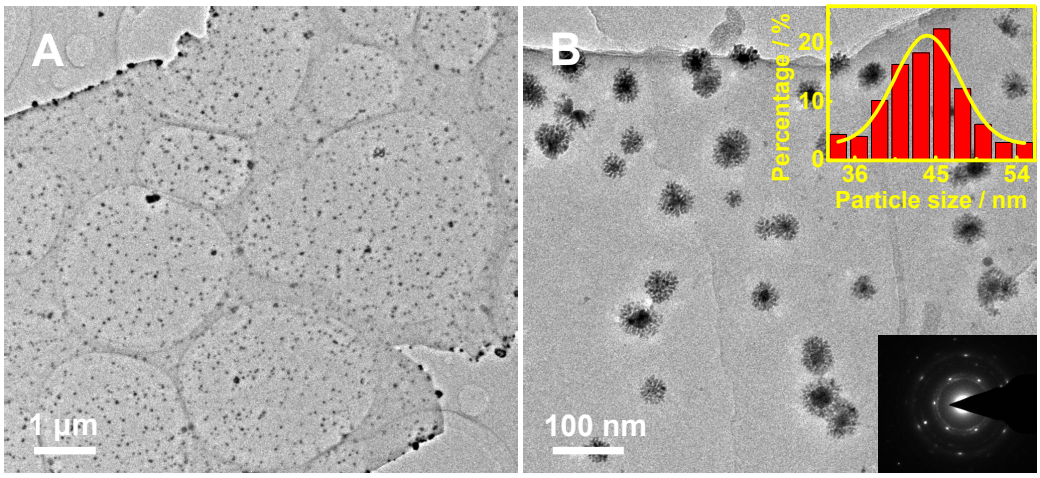

Fig. 2

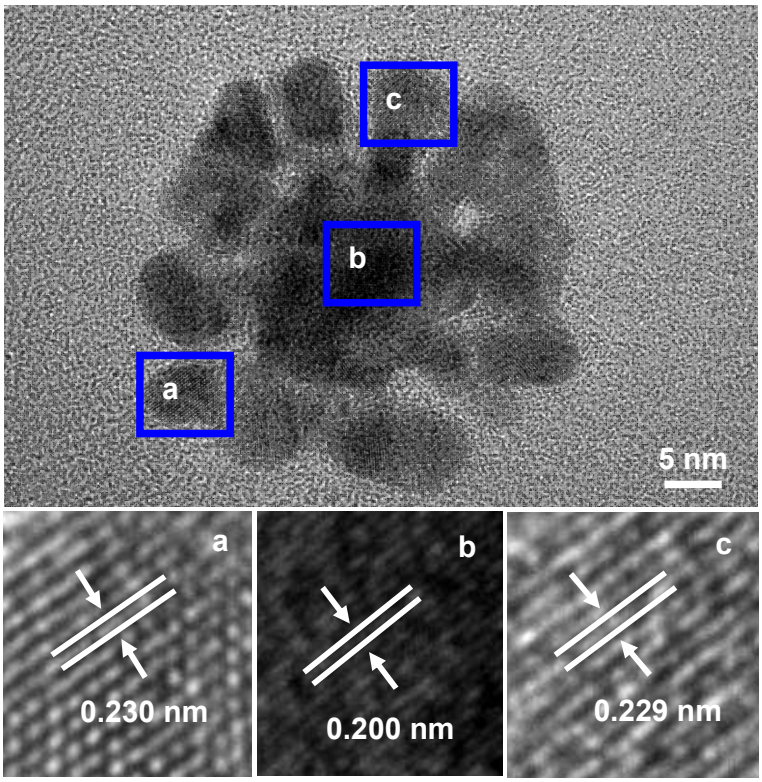

Fig. 3

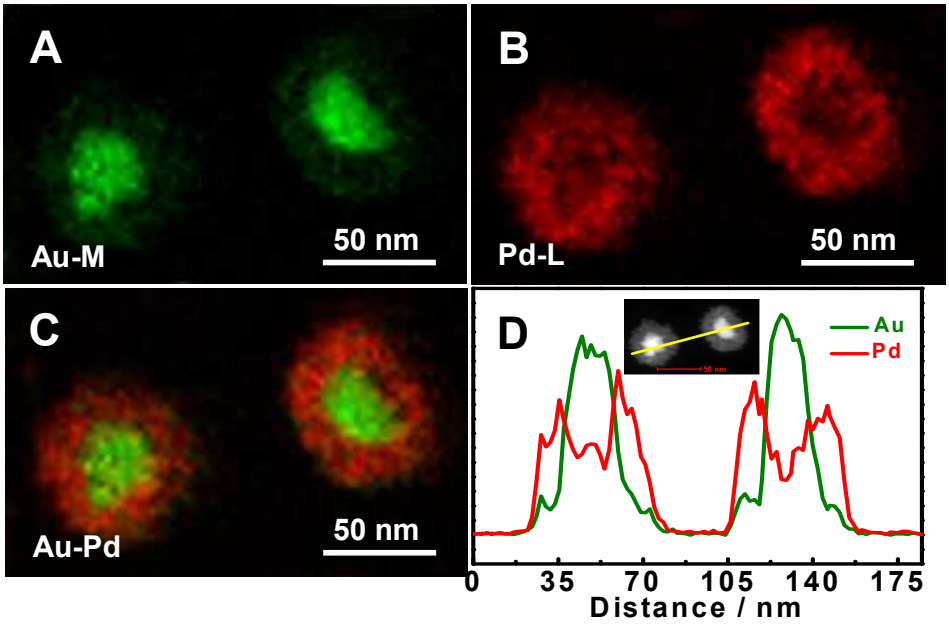

Fig. 4

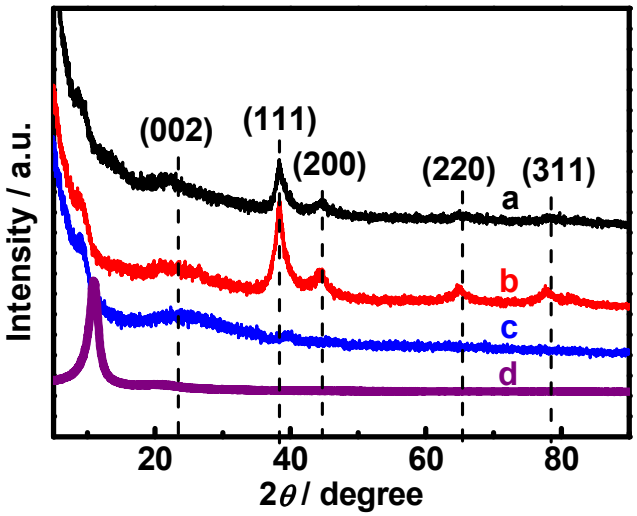

Fig. 5

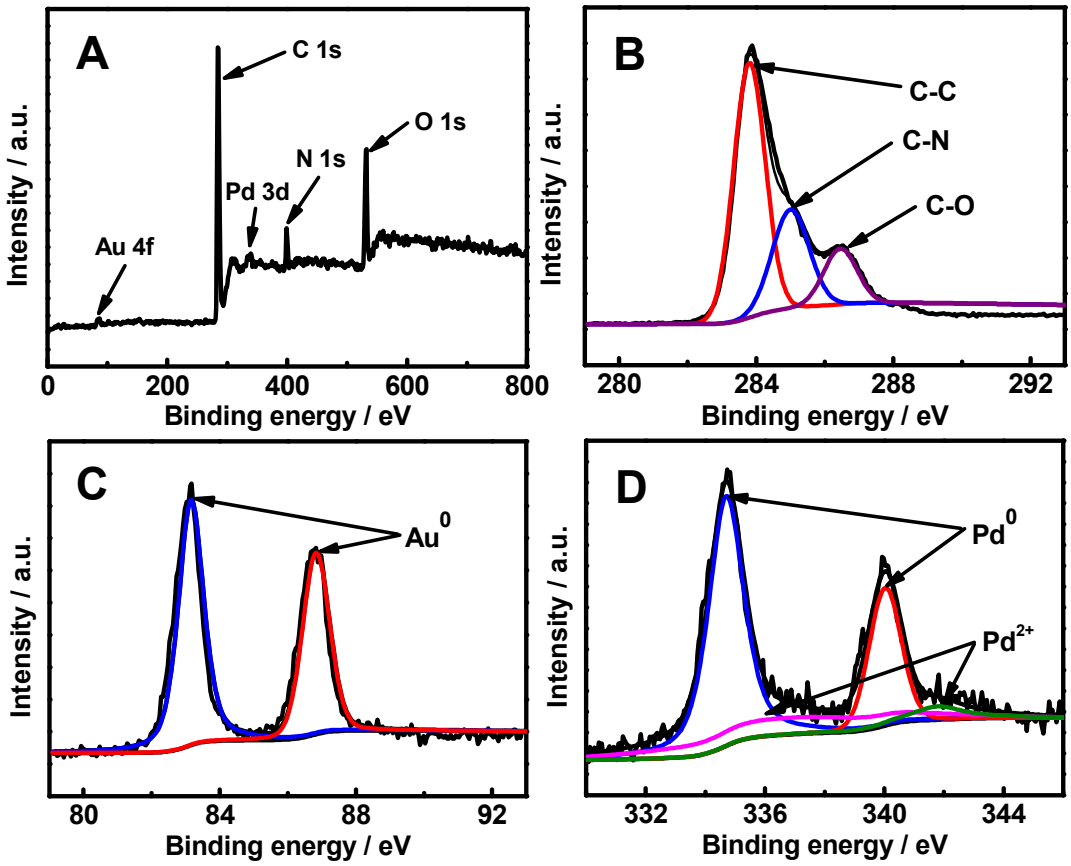

Fig. 6

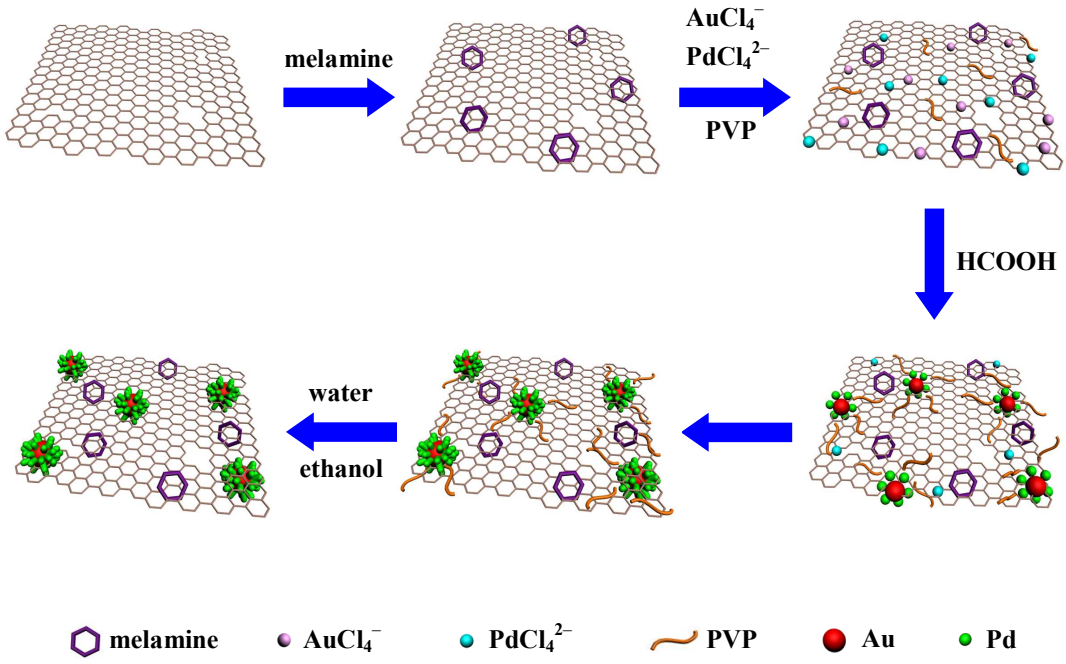

Fig. 7

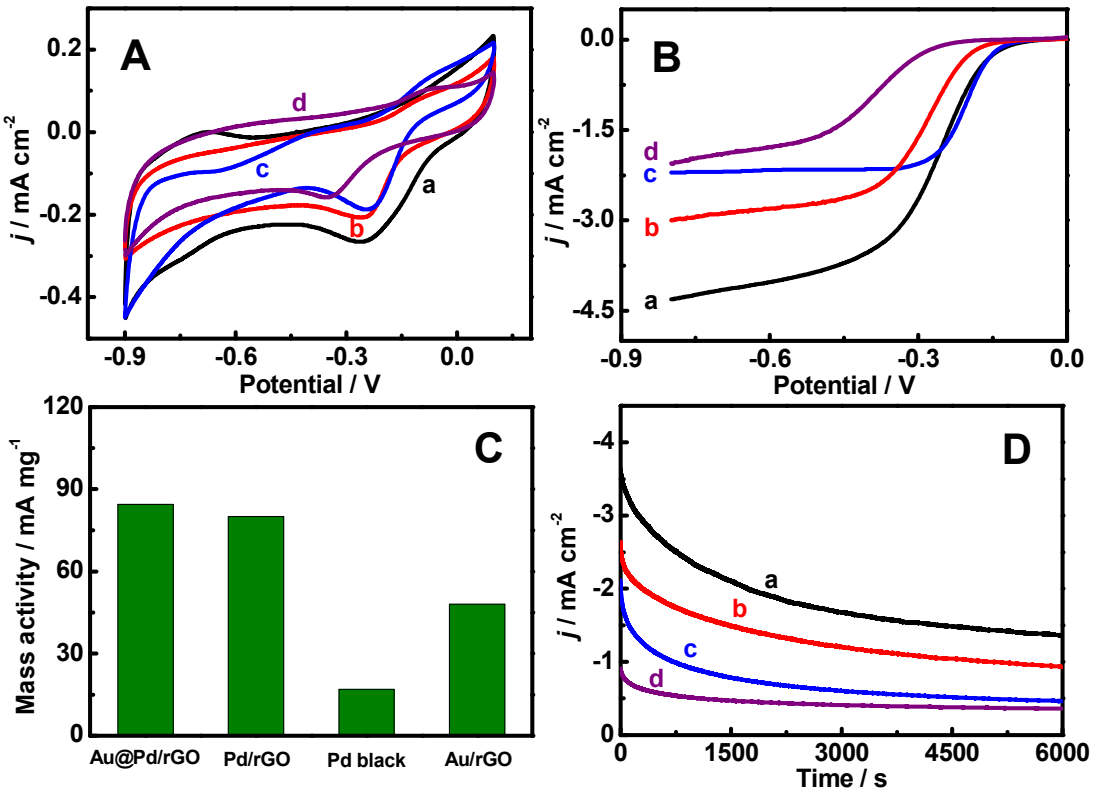

Fig. 8

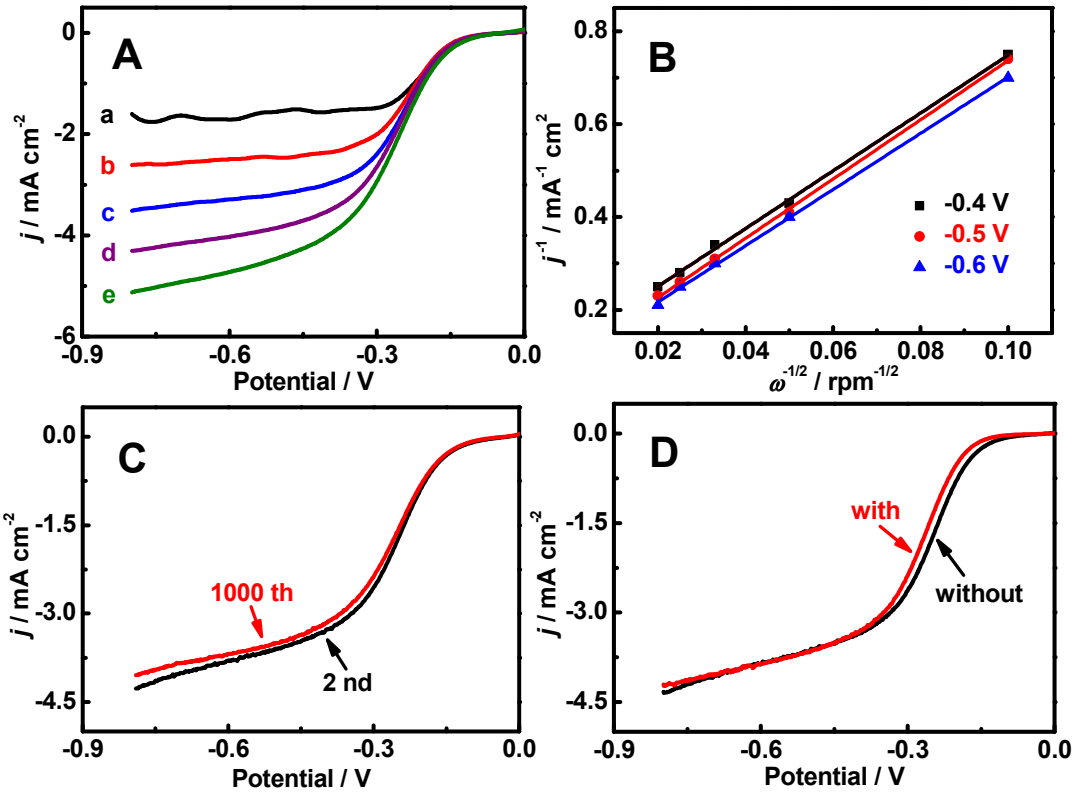

Fig. 9